scientific reports

Check for updates

OPEN

Structural characterization of metal binding in human tyrosylprotein sulfotransferase 2, TPST2

Minwoo Jin[1,2], Chaemin Noh[1,2], Jihyeong Yang[1,2], Hyunwoo Kim[1,2], Soo Bin Park[1], Yong-Chul Kim[1] & Soo Hyun Eom[1,2,3]✉

Tyrosylprotein sulfotransferases (TPSTs) catalyze O-sulfation of tyrosine residues on secreted and membrane proteins, but the molecular basis for their stimulation by metal ions remains unclear. We determined the structures of the catalytic domain of human TPST2 with PAP and Na^+ (1.75 Å) or Mn^{2+} (2.00 Å) bound and identified two conserved octahedral metal-binding sites. Anomalous diffraction at metal absorption edges confirmed the identity of the bound metals and demonstrated specific Mn^{2+} binding. The Na^+- and Mn^{2+}-bound structures closely superimposed, suggesting activation without large conformational changes. Structural comparison with the apo structure and ensemble refinement revealed differences in local dynamics around the metal binding sites. The flexible α3-helix and α12-α13 loop in the apo structure were stabilized by Na^+ binding and further rigidified by Mn^{2+} binding. These findings support an activation-by-ordering mechanism in which Na^+ binding generates a pre-activated state, with Mn^{2+} subsequently establishing a catalytically competent ordering that lowers the entropic barrier at the active-site entrance. This framework reconciles longstanding biochemical observations and suggests that Mn^{2+} availability within the Golgi can tune TPST2-dependent signaling.

Tyrosylprotein sulfotransferases (TPSTs) are enzymes localized within the trans-Golgi network and catalyze post-translational O-sulfation of tyrosine residues[1–3]. Using the universal sulfate donor 3′-phosphoadenosine-5′-phosphosulfate (PAPS), TPSTs transfer a sulfonyl group to the phenolic oxygen of tyrosine to form a tyrosine O-sulfate ester and 3′-phosphoadenosine-5′-phosphate (PAP)[1,4,5] (Fig. 1). Protein tyrosine sulfation is widespread in metazoans, occurring predominantly along the secretory pathway[6–8], where it modulates extracellular protein-protein recognition in diverse extracellular interactions, including hemostasis, leukocyte rolling and adhesion, chemokine-receptor signaling, viral entry, and hormone-receptor interaction[9–11].

Two human TPST isoforms, TPST1 (370 aa) and TPST2 (377 aa), have been identified. Both adopt the type II membrane protein topology with a short cytosolic N-terminus, single transmembrane helix, and luminal catalytic domain[12–14], and share the canonical sulfotransferase fold containing the conserved 5′-phosphosulfate binding (5′-PSB) and 3′-phosphate binding (3′-PB) motifs[15–17] (Supplementary Fig. 1). Biochemical and mutational studies have shown that TPSTs preferentially recognize acidic sequence motifs flanking the acceptor Tyr site, with Asp/Glu residues within ± 5 positions[18–20]. The high-resolution crystal structure of human TPST2 bound to PAP and a C4-derived peptide (C4P5Y3) defined the peptide-binding cleft and clarified the catalytic mechanism of the tyrosine sulfation[16]. Complementary analyses of human TPST1 structures, together with enzymatic characterization, provided additional insight into their substrate specificity and isoform-dependent differences in recognition[17]. More recently, the crystal structure of tick TPST in complex with PAP and a madanin-derived peptide revealed a sequential sulfation mechanism in which sulfation of Tyr51 facilitates subsequent modification of Tyr54, providing comparative insight into substrate recognition across TPSTs[21]. Together, these structural studies characterize the molecular framework of TPST isoforms and highlight the conserved catalytic features underlying substrate recognition and function.

TPST2 exhibits distinct physiological and pathological properties. *Tpst2*-deficient mice exhibit primary hypothyroidism, growth delay and male infertility, which demonstrate the enzyme's essential contribution to thyroid hormone biosynthesis and reproductive function[22–24]. TPST1 and TPST2 differ in their tissue

[1]Department of Life Sciences, Gwangju Institute of Science and Technology (GIST), Gwangju, Republic of Korea. [2]Steitz Center for Structural Biology, Gwangju Institute of Science and Technology (GIST), Gwangju, Republic of Korea. [3]Department of Chemistry, Gwangju Institute of Science and Technology (GIST), Gwangju, Republic of Korea. ✉email: eom@gist.ac.kr

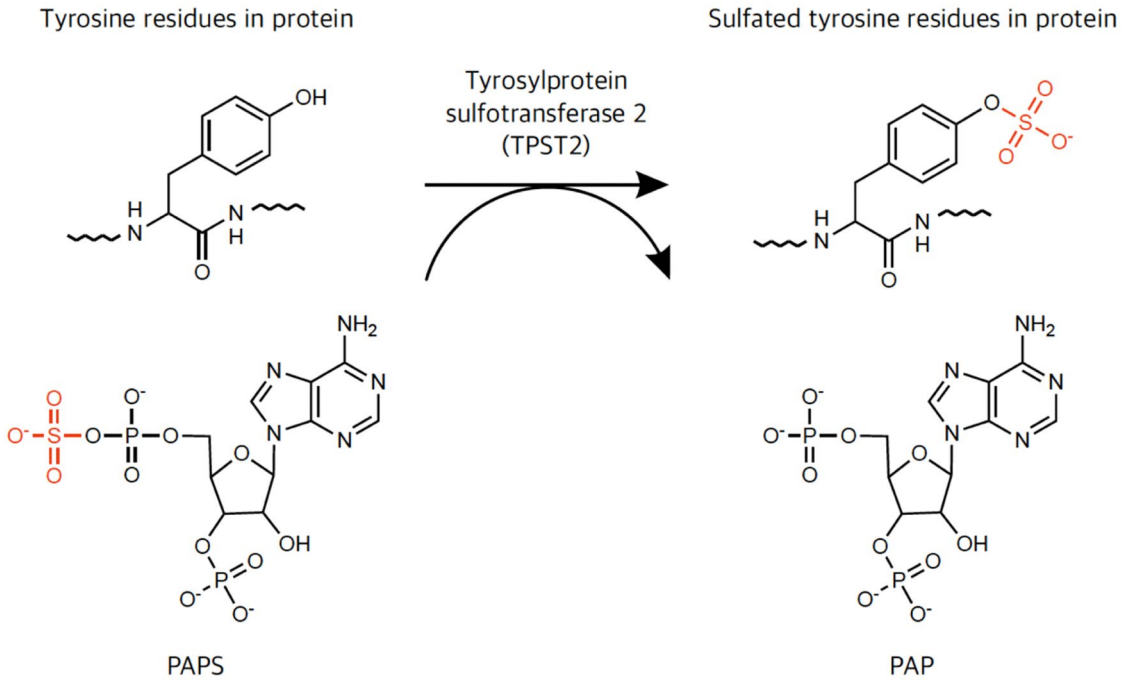

Fig. 1. Tyrosylprotein sulfation reaction catalyzed by TPST2. Schematic illustration of the PAPS-dependent sulfation reaction catalyzed by TPST2. The sulfonyl group from PAPS is transferred to the hydroxyl group of tyrosine to generate tyrosine O-sulfate and PAP.

distributions and enzymatic properties, which is consistent with their isoform-specific substrate preferences[17,25]. In addition, recent studies have shed light on the significance of TPST2 in disease. In melanoma, for example, TPST2 sulfates IFNGR1 at Tyr397 to suppress IFN-ɣ signaling, and the absence of TPST2 enhances the efficacy of PD-1 blockade, implicating the enzyme in tumor immune evasion[26]. In pancreatic ductal adenocarcinoma, the SLC35B2-TPST2 axis promotes tumor growth and metastasis, with integrin β4 identified as a TPST2 substrate whose sulfation stabilizes the protein[27]. Conversely, TPST2 inhibition reduces cancer cell proliferation, migration, invasion and metastasis. In parallel, the recent development of antibodies that specifically recognize sulfotyrosine provides powerful tools for probing TPST-mediated signaling in physiological and pathological contexts[28]. These findings establish TPST2 as a critical regulator of extracellular signaling and tumor biology and underscore the need to define the molecular basis of its regulation.

A characteristic biochemical property of TPSTs is stimulation by divalent metals[18,19,29,30]. Early enzymatic assays demonstrated that tyrosine sulfation is markedly enhanced in the presence of Mn^{2+} or Mg^{2+}, indicating the requirement of divalent ions for maximal activity[18,19]. Assays with recombinant enzymes revealed that activation is isoform specific with TPST2, but not TPST1, responsive to Mg^{2+}, and the optimal $MnCl_2$ level and maximal activation differing between the two isoforms[25]. Comparative enzymology further revealed that Mn^{2+} significantly enhances the catalytic efficiency of human TPST2. Optimal activity for some substrates was observed at low millimolar concentrations of $MnCl_2$, though the extent of the stimulation depended strongly on the peptide sequence and buffer composition[30]. Despite these biochemical observations, the molecular basis of metal activation remains unclear, and a structural framework for understanding how Mn^{2+} enhances TPST2 activity has not been established. These uncertainties highlight the necessity for direct structural and dynamics-based investigations into metal binding to TPST2.

Here, we determined the crystal structures of human TPST2 with mono- and divalent metal ions. We determined their ion specificities through anomalous diffraction analysis for Mn^{2+}, Co^{2+}, Zn^{2+} and Cu^{2+}, and we assessed local flexibility using per-residue root-mean-square fluctuation (RMSF) analysis. Our results demonstrate that Mn^{2+} and Co^{2+} selectively occupy two conserved octahedral sites, reduce conformational fluctuations in the α3-helix and α12-α13 loop, and enhance local stability without inducing global structural changes. These findings provide a structural basis for understanding the metal-dependent activation of TPST2 and support a model in which divalent metal binding reduces the entropic barrier for catalysis by stabilizing key elements of the active site.

Results

Structure determination of Na^+-bound TPST2 and identification of two metal-binding sites

The catalytic domain of human TPST2 (residues 43–359; *h*TPST2) was overexpressed in *E. coli* (Fig. 2a and Supplementary Fig. 2a). The enzymatic activity of *h*TPST2 was assessed in an in vitro sulfotransferase assay, which confirmed that the recombinant catalytic domain retained activity in the absence of the transmembrane anchor and cytosolic tail (Supplementary Fig. 3). To obtain diffraction-quality crystals of *h*TPST2, co-crystallization with PAP was essential. We determined the structure of Na^+-bound TPST2 ($TPST2^{Na}$) in complex with PAP at 1.75 Å resolution using molecular replacement with R_{work} and R_{free} values of 17.1% and 18.7%, respectively (Table 1).

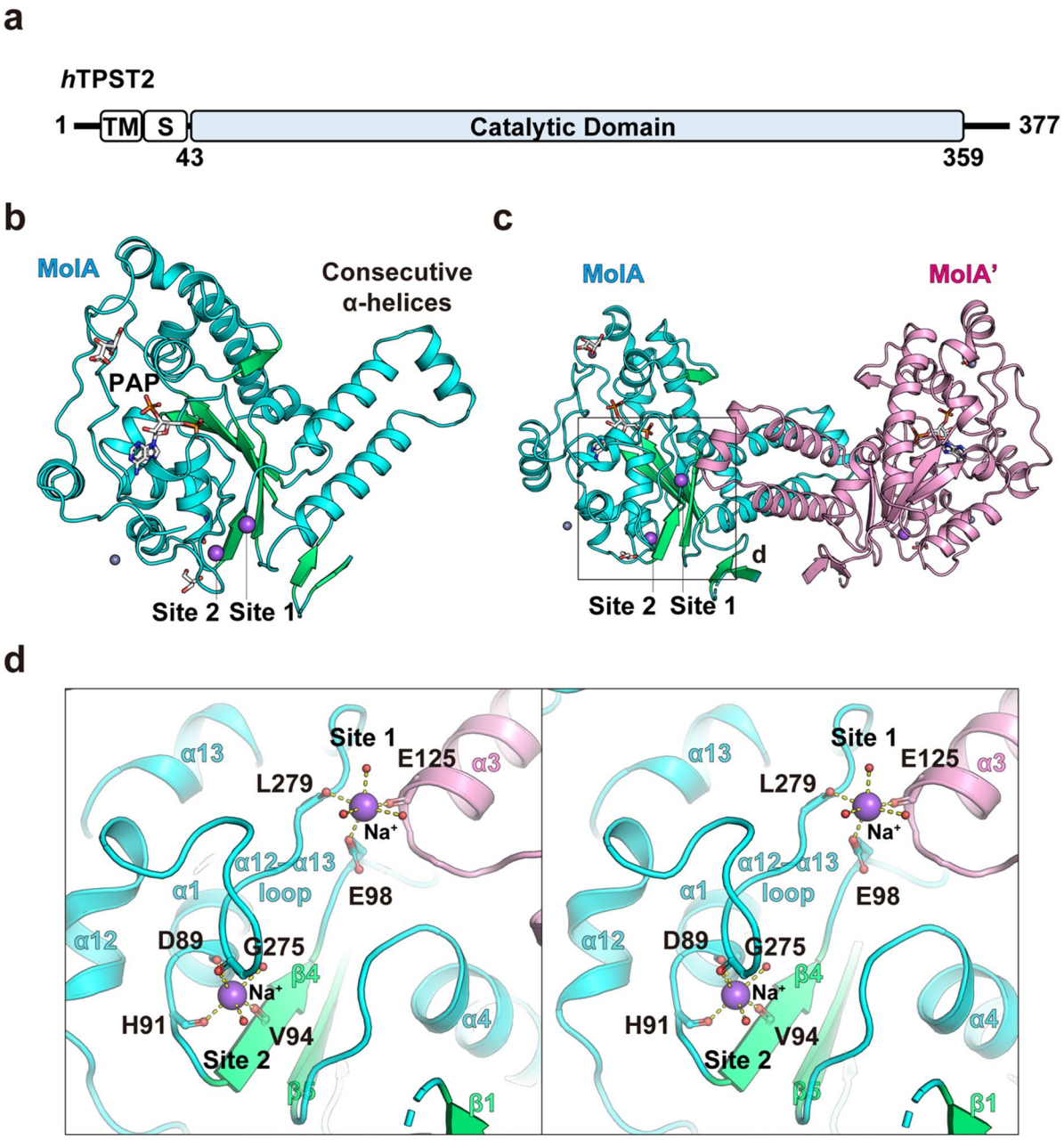

Fig. 2. Overall structure of TPST2 in the cation-bound state. (**a**) Domain organization of human TPST2, which consists of a transmembrane helix (TM), stem region (S) and luminal catalytic domain. The catalytic domain used for crystallization is colored cyan. **b**, **c** Cartoon representations of $TPST2^{Na}$ monomer (**b**) and dimer (**c**). The two protomers are colored cyan and pink, with β-sheets highlighted in lime green. Bound Na^+ and Zn^{2+} ions are shown as purple and gray spheres, respectively. PAP, glycerol (GOL), and tartrate (TLA) are shown as white sticks. **d** Stereo view of cation-binding sites 1 and 2. Coordinating residues are shown as sticks, Na^+ ions as purple spheres, and water molecules are red spheres.

	TPST2^{Na} (PDB: 9WWE)	TPST2^{Mn} (PDB: 9WWF)	Mn (ano)	Co (ano)	Zn (ano)	Cu (ano)
Data collection						
Wavelength (Å)	1.0000	0.9794	1.8933	1.6054	1.2824	1.3785
Space group	$P4_122$	$P4_122$	$P4_122$	$P4_122$	$P4_122$	$P4_122$
Unit cell: a, b, c (Å) α, β, γ (°)	102.3, 102.3, 103.6 90.0, 90.0, 90.0	102.8, 102.8, 103.1 90.0, 90.0, 90.0	102.8, 102.8, 103.0 90.0, 90.0, 90.0	102.6, 102.6, 103.7 90.0, 90.0, 90.0	102.6, 102.6, 104.0 90.0, 90.0, 90.0	102.8, 102.8, 102.8 90.0, 90.0, 90.0
Resolution range (Å)	46.2–1.75 (1.79–1.75)	46.1–2.00 (2.05–2.00)	46.1–2.20 (2.27–2.20)	46.3–2.30 (2.38–2.30)	50.0–2.30 (2.34–2.30)	50.0–2.40 (2.44–2.40)
R_{merge} [a]	14.4 (123.5)	17.6 (84.0)	16.6 (85.2)	16.8 (100.1)	20.2 (122.1)	22.8 (97.1)
R_{pim}	2.8 (24.1)	3.6 (17.0)	3.5 (25.1)	3.4 (20.1)	4.1 (25.3)	4.6 (22.4)
$CC_{1/2}$	0.999 (0.760)	0.999 (0.873)	0.998 (0.700)	0.999 (0.908)	0.982 (0.873)	0.977 (0.871)
$I/\sigma(I)$	18.7 (3.5)	24.4 (10.8)	16.0 (3.2)	19.5 (4.3)	20.5 (2.7)	17.4 (2.1)
Completeness (%)	100.0 (99.2)	99.9 (99.3)	99.2 (92.3)	100.0 (99.7)	100.0 (100.0)	99.9 (99.4)
Redundancy	26.8 (26.3)	25.0 (25.1)	23.0 (11.8)	25.2 (25.5)	25.5 (24.2)	24.6 (18.4)
Refinement						
Resolution (Å)	46.2–1.75	46.1–2.00				
No. unique reflections	55,401 (3864)	37,847 (2860)				
R_{work}/R_{free} [b] (%)	17.0/18.6	18.3/22.6				
No. atoms	2682	2686				
Protein	2377	2359				
Ligands	47	42				
Solvent	258	285				
B-factors						
Protein	23.4	17.5				
Ligands	22.8	27.9				
Solvent	34.0	30.9				
R.m.s. deviations						
Bond lengths (Å)	0.006	0.007				
Bond angles (°)	1.23	1.22				
Ramachandran plot (%)						
Favored/allowed/disallowed	98.3/1.7/0.0	98.0/2.0/0.0				

Table 1. Data collection and refinement statistics. Values in parentheses are for the highest resolution shell. [a]$R_{merge} = \Sigma h \Sigma i \mid I(h)i - \langle I(h) \rangle \mid / [\Sigma h \Sigma i\, I(h)i]$, where I(h) is the intensity of reflection of h, Σh is the sum over all reflections, and Σi is the sum over i measurements of reflection h. [b]$R_{work} = \Sigma hkl \mid\mid Fo \mid - \mid Fc \mid \mid / (\Sigma hkl \mid Fo \mid)$; 5% of the reflections were excluded for the R_{free} calculation.

Inspection of σ_A-weighted mF_o-DF_c maps above 8σ revealed two well-ordered metal densities with octahedral coordination geometry, hereafter referred to as metal-binding site 1 and site 2 (Fig. 2b; Table 2). To evaluate which metals were most plausible at sites 1 and 2, we analyzed both positions using the CheckMyMetal[31] (CMM) and MetalPDB[32] servers. CMM analysis favored Na^+ assignments for both metal-binding sites, with all stereochemical and geometric parameters within acceptable or borderline ranges for Na^+ (Supplementary Fig. 4). When K^+ was modeled at this position, the refined B factor of the ion (~ 32 $Å^2$) was substantially greater than those of the coordinating atoms and surrounding residues. In addition, average coordination distances (2.6 Å) and B-factor ratios were consistent with Na^+. Taken together with the high sodium content of the mother liquor (~ 120 mM), we modeled two metal-binding sites as Na^+ within TPST2^{Na}.

The TPST2^{Na} monomer consisted of three consecutive α-helices and a single α/β motif with a five-stranded parallel β-sheet (Fig. 2b). PAP occupied the canonical 5′-PSB and 3′-PB subsites in a pose consistent with previously reported human TPST2 structures[16] (Supplementary Fig. 5). Two lattice-associated metal densities were identified at crystal-packing interfaces but were not positioned to contribute directly to catalysis (Supplementary Fig. 6). The asymmetric unit contained one TPST2 protomer, and the physiological dimer was generated by crystallographic symmetry (Fig. 2c). Together, these results establish a well-ordered PAP-bound TPST2^{Na} structure with two coordinated Na^+ ions positioned within the catalytic domain.

Structural conservation and divergence of TPST2 metal-binding sites

We next examined the coordination environments of the two metal-binding sites (Fig. 2d). Site 1 was located near the C-terminus of the α3-helix at the dimer interface. Its coordination sphere comprised the Glu98 side chain, main-chain carbonyl oxygens of Glu125 and Leu279, and three water molecules. Site 2 was positioned near the C-terminus of the α1-helix, adjacent to the 5′-PSB region. This site was coordinated by main-chain carbonyl oxygens from Asp89, His91, Val94 and Gly275 together with two water molecules. The structural

	TPST2^{Na} (PDB: 9WWE)	TPST2^{Mn} (PDB: 9WWF)	TPST2^{pep} (PDB: 3AP1)	TPST2^{apo} (PDB: 3AP3)	Co (ano)	Zn (ano)	Cu (ano)
Cation concentration (mM)							
Na	120	120	300	200	120	120	120
K	100	100	-	-	100	100	100
Zn	25	1	-	-	1	10	1
Mn	-	20	1	1	-	-	-
Co	-	-	-	-	10	-	-
Cu	-	-	-	-	-	-	10
Peak height ($2F_o$–F_c / anomalous; σ)							
Metal binding site 1	8.1 / NA	5.8 / 8.5	2.6 / -	- / -	5.1 / 5.2	4.3 / -	3.7 / -
Metal binding site 2	10.1 / NA	7.6 / 5.8	5.2 / -	- / -	4.5 / 3.5	4.3 / -	3.4 / -
Crystallographic lattice site 1	28.5 / NA	23.3 / 10.7	- / -	- / -	16.8 / 5	13.3 / 46.0	14.6 / -
Crystallographic lattice site 2	20.3 / NA	- / -	- / -	- / -	- / -	4.2 / 9.3	- / -

Table 2. Crystallization conditions and electron density features of TPST2 structures. Values indicate crystallization cation concentrations and corresponding $2F_o$-F_c / anomalous peak heights (σ) observed at metal-binding or lattice sites.

definition of the two metal-binding sites in TPST2 provides a framework with which to evaluate the conservation of coordinating residues across TPST homologs.

We analyzed representative TPST sequences and compared the TPST2^{Na} structure with TPST1 (PDB 5RWI) and tick TPST (PDB 8W5Z) structures (Fig. 3a and b). Site 1 residues (Glu98, Glu125, and Leu279) were strictly conserved across TPST homologs, which is consistent with an invariant coordination environment. This site was clearly occupied by Na^+, whereas other TPST structures had not assigned a metal at this position. These findings indicate that although site 1 is strongly conserved, it is associated with a comparatively dynamic coordination environment. Consistent with this interpretation, CMM analysis showed higher B-factors for both the Na^+ ion and its coordinating residues at site 1 than site 2 (site 1: 21.7 and 34.5; site 2: 17.0 and 20.3) (Supplementary Fig. 4).

The loop region surrounding site 2 showed notable divergence. While TPST2 and TPST1 shared well-superimposed coordinating residues, the tick TPST exhibited a shortened α12-α13 loop and lacked the conserved Gly275 that participates in metal coordination at site 2 (Fig. 3b). Nevertheless, in all three structures the ligands around site 2 assumed a comparable octahedral coordination geometry (Supplementary Fig. 7). Broader sequence alignments further revealed that in invertebrate homologs, this region is either truncated or lacking the equivalent Gly275 (Fig. 3a). These observations suggest that, although the local coordination environment of site 2 is conserved, the surrounding loop region is more variable than at site 1 and may contribute to species-dependent differences in metal-dependent activation.

Metal-binding profile by single-wavelength anomalous diffraction

Biochemical assays have established that Mn^{2+} strongly activates TPST2 activity[25,30]. To structurally define this effect, we determined the Mn^{2+}-bound structure (TPST2^{Mn}) in complex with PAP at 2.00 Å resolution and R_{work} and R_{free} values of 18.3% and 22.5%, respectively (Table 1; Fig. 4a). We also collected single-wavelength anomalous diffraction (SAD) data at the Mn K-edge (λ = 1.8933 Å) (Table 1). The anomalous difference map displayed two strong peaks corresponding to metal-binding sites, 8.5σ at site 1 and 5.8σ at site 2 (Fig. 4b). The corresponding $2F_o$-F_c map densities were 5.8σ and 7.6σ, respectively. These results indicate that Mn^{2+} occupied both sites. The relative difference between the anomalous and $2F_o$-F_c peak heights further suggested that site 1 had higher occupancy but exhibited greater mobility, while site 2 had lower occupancy within a more rigid coordination environment.

To probe ion selectivity, we collected additional SAD datasets from TPST2^{Na} crystals soaked with 10 mM $CoCl_2$, $ZnCl_2$ or $CuCl_2$ at wavelengths close to the K-edge of each element (λ = 1.6054 Å, 1.2824 Å, and 1.3785 Å, respectively) (Table 1). Anomalous difference Fourier maps were then inspected at the metal-binding sites to assess the presence of metal-specific signals (Table 2). Fourier-difference anomalous maps displayed Co^{2+} signals of 5.2σ at site 1 and 3.5σ at site 2 (Supplementary Fig. 8). Zn^{2+} produced no signal at either site but instead localized to packing sites enriched in histidine and acidic residues (Supplementary Fig. 9). Cu^{2+} datasets showed only weak (< 2σ) and spatially diffuse peaks inconsistent with specific binding. Structural alignment of TPST2^{Na}, TPST2^{Mn}, and soaking structures showed nearly identical coordinates with a monomer root mean square deviation (RMSD) of ~ 0.1 Å and dimer RMSD of ~ 0.2 Å (Supplementary Fig. 10). Those findings indicate that TPST2 did not undergo large conformational changes upon metal binding. Thus, the anomalous mapping established that TPST2 selectively binds Mn^{2+} at its two sites, though it also weakly binds Co^{2+}. Zn^{2+} and Cu^{2+} failed to occupy these positions. This selectivity is consistent with biochemical kinetic observations that Mn^{2+} strongly activated TPST2[25], while Zn^{2+} produced little stimulation of enzymatic activity[29].

Comparisons with metal unbound TPST2 structures

To further assess the impact of Mn^{2+} binding, we compared TPST2^{Mn} with previously reported human TPST2 structures representing peptide-bound (TPST2^{pep}, PDB 3AP1) and apo (TPST2^{apo}, PDB 3AP3) states. Monomer

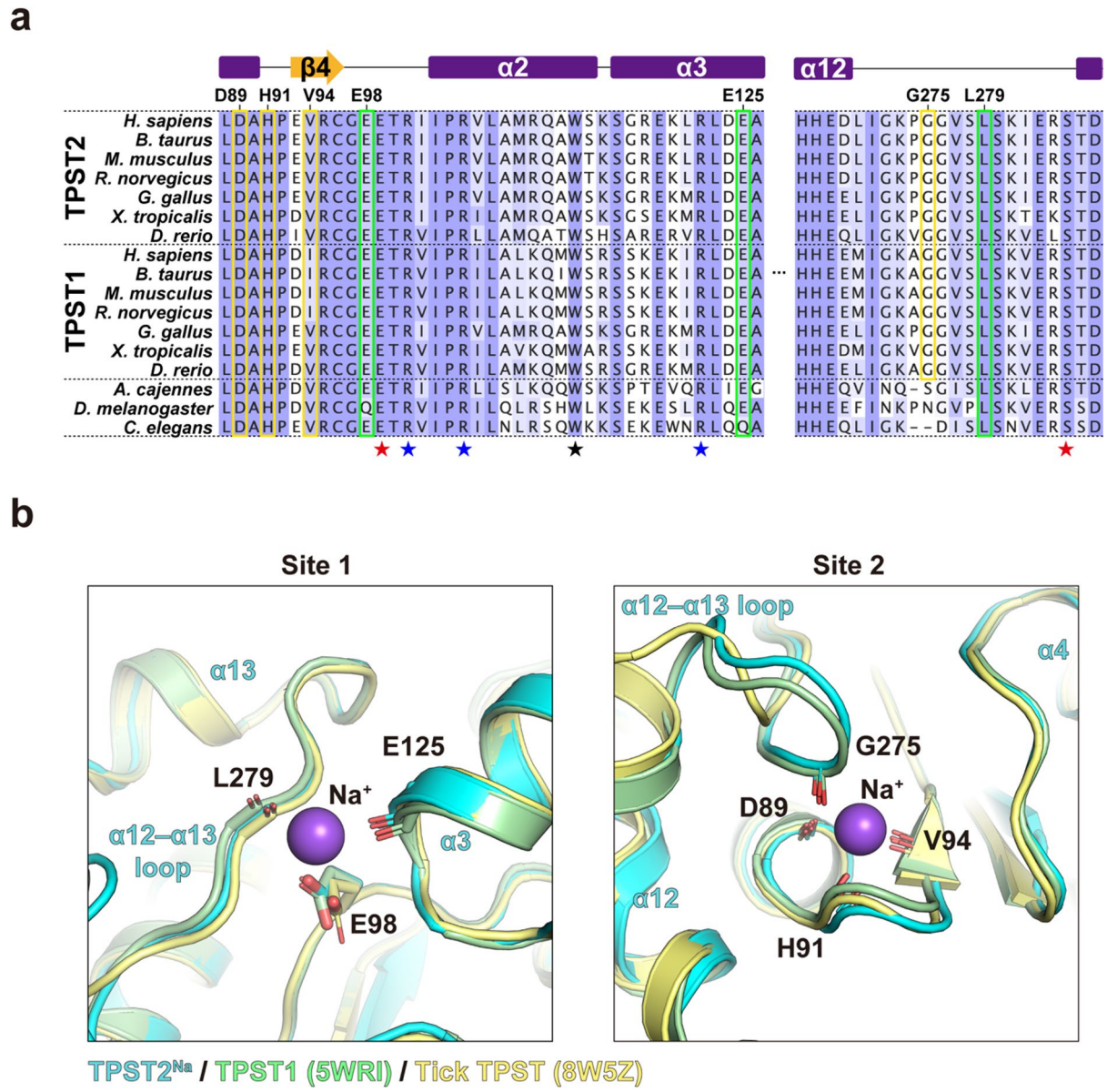

Fig. 3. Conservation of cation binding sites across TPST homologs. (**a**) Multiple sequence alignment of TPST homologs highlighting residues forming cation-binding sites 1 and 2. Coordinating residues at sites 1 and 2 are boxed in green and yellow, respectively. Catalytic residues, peptide-binding residues, and dimerization-related residues are marked with red, blue and black stars, respectively. Sequence conservation is represented by a purple gradient. **b** Detailed view of superimposed cation-binding sites 1 and 2 in human TPST2^{Na} (cyan), TPST1 (green; PDB 5WRI) and tick TPST (yellow; PDB 8W5Z). Na^+ ions are shown as purple spheres, and coordinating residues are depicted as sticks.

overlays revealed small RMSDs (~0.3 Å), confirming that the catalytic core remained pre-organized across PAP-bound states (Fig. 5a; Table 3). However, when we aligned one protomer of the dimer, the opposing catalytic domain of the protomer displayed a modest rigid-body shift of ~3–6 Å among states (Fig. 5b). The TPST2^{apo} structure positioned the opposing catalytic domain lowest, whereas the TPST2^{Mn} and TPST2^{pep} structures shifted the protomer toward the substrate peptide cleft.

Within the TPST2^{pep} structure, a short βe has an antiparallel interaction with the substrate peptide. By contrast, within the TPST2^{Mn} and TPST2^{apo} structures, which lacked a substrate peptide, βe was positioned farther from the cleft (Fig. 5c). The TPST2^{Mn} structure differed in that the α12-α13 loop shifted toward the active site and stabilized the α3-helix in an ordered conformation, despite the absence of the substrate peptide (Fig. 5c). At site 1, the α12-α13 loop was positioned closer to the α3-helix in TPST2^{Mn} than in the other structures, which shortened the carbonyl-oxygen distance between Glu125 and Leu279 (4.4 Å vs. 5.3 and 5.1 Å) (Fig. 5d). Furthermore, site 1 was located at the C-terminal end of the α3-helix, suggesting that Mn^{2+} binding stabilizes the

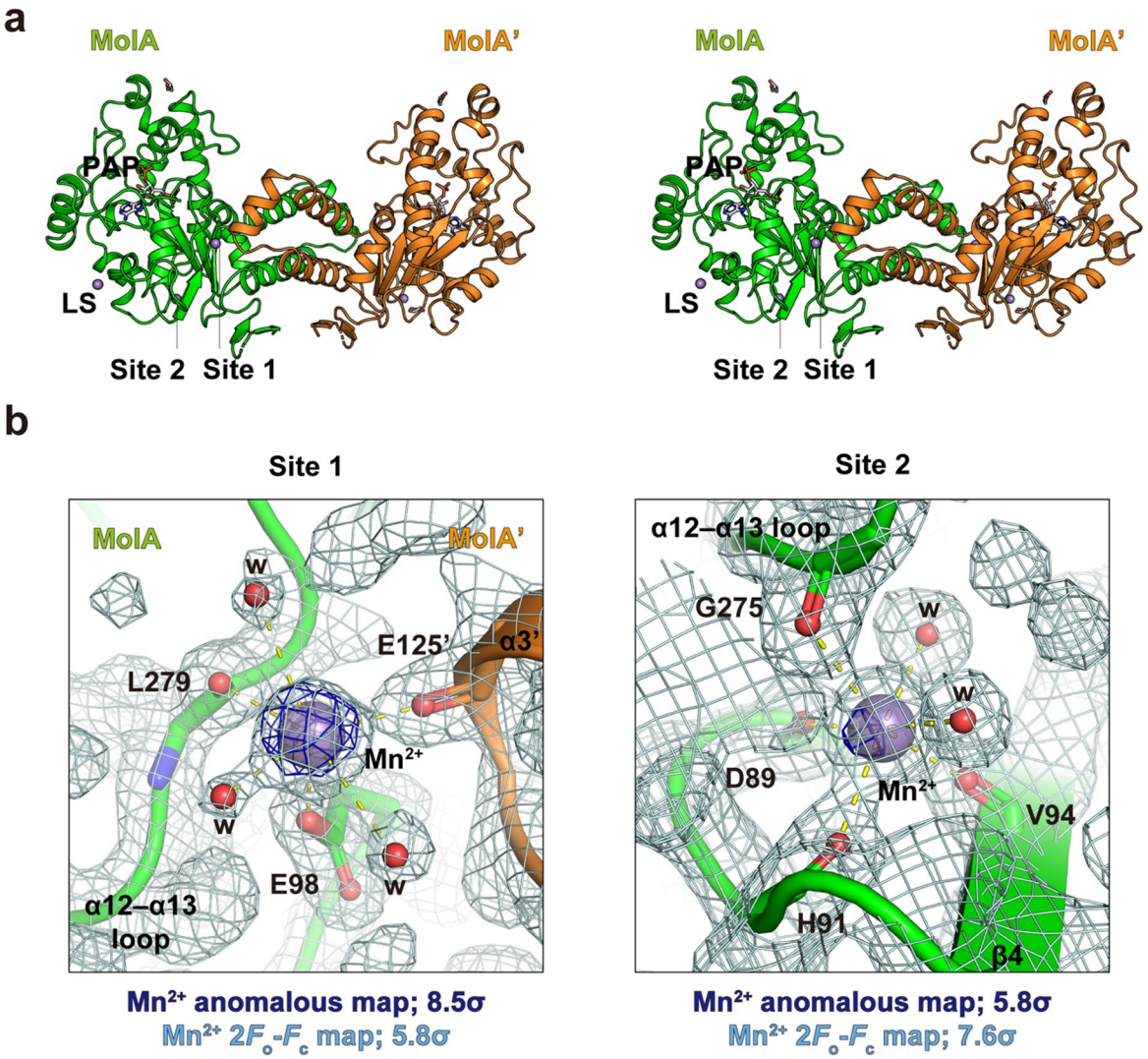

Fig. 4. Selective Mn^{2+} binding detected by anomalous diffraction in TPST2. (**a**) Stereo view of the $TPST2^{Mn}$ dimer structure shown as a cartoon representation. The two protomers are colored green and orange. Site 1; cation-binding site 1, Site 2; cation-binding site 2, LS; crystallographic lattice site 1 (**b**) Close-up view of cation-binding sites 1 and 2 in human $TPST2^{Mn}$. Mn^{2+} anomalous and $2F_o$-F_c electron density maps are shown in dark blue and light blue, respectively. The anomalous map is contoured at 5.0 σ, and the $2F_o$-F_c map at 1.5 σ, with peak heights labeled below. Bound Mn^{2+} ions are shown as light violet transparent spheres, and coordinating residues are represented as sticks. Water molecules are depicted as red spheres and labeled w.

helix dipole. Consistent with that interpretation, the α3-helix was disordered in the $TPST2^{apo}$ structure, and the α2-α3 kink (residues 112–117) also adopted multiple conformations within the $TPST2^{pep}$ structure[16].

These observations indicate that Mn^{2+} binding at site 1 stabilizes the dimer interface and preserves the integrity of the α3-helix without introducing large-scale conformational rearrangements. Notably, previous TPST2 structures were crystallized under high Na^+ conditions (>200 mM), yet no Na^+ ions were modeled at the binding sites, and the α3-helix appeared less ordered. This likely reflects incomplete or heterogeneous Na^+ occupancy together with resolution limitations, rather than a true absence of bound ions. By contrast, our $TPST2^{Na}$ structure captured clear ion densities and displayed a stabilized α3-helix. These observations indicate that sufficient cation occupancy can promote structural ordering and suggest that our Na^+-bound structure represents a cation-stabilized form of TPST2.

Metal-dependent dynamics and stability

To further validate the stabilizing effect of metal binding indicated by the structural comparisons, we next examined the thermal stability of *h*TPST2 under Na^+- and Mn^{2+}-bound conditions. The melting temperature (T_m) of *h*TPST2 in the Mn^{2+}-bound state (Mn; 49.7 ± 0.3 °C) was higher than in the Na^+-bound state (Na; 47.6 ± 0.1 °C) (Fig. 6a). We then performed ensemble refinement followed by per-residue RMSF analysis with Z-normalization (Z-RMSF) (Fig. 6b). Two regions showed lower Z-RMSF upon metal binding: the α3 helix (residue 109–126) and the α12-α13 loop (residue 261–285) (Fig. 6c). Notably, Ser116 at the α2-α3 kink and

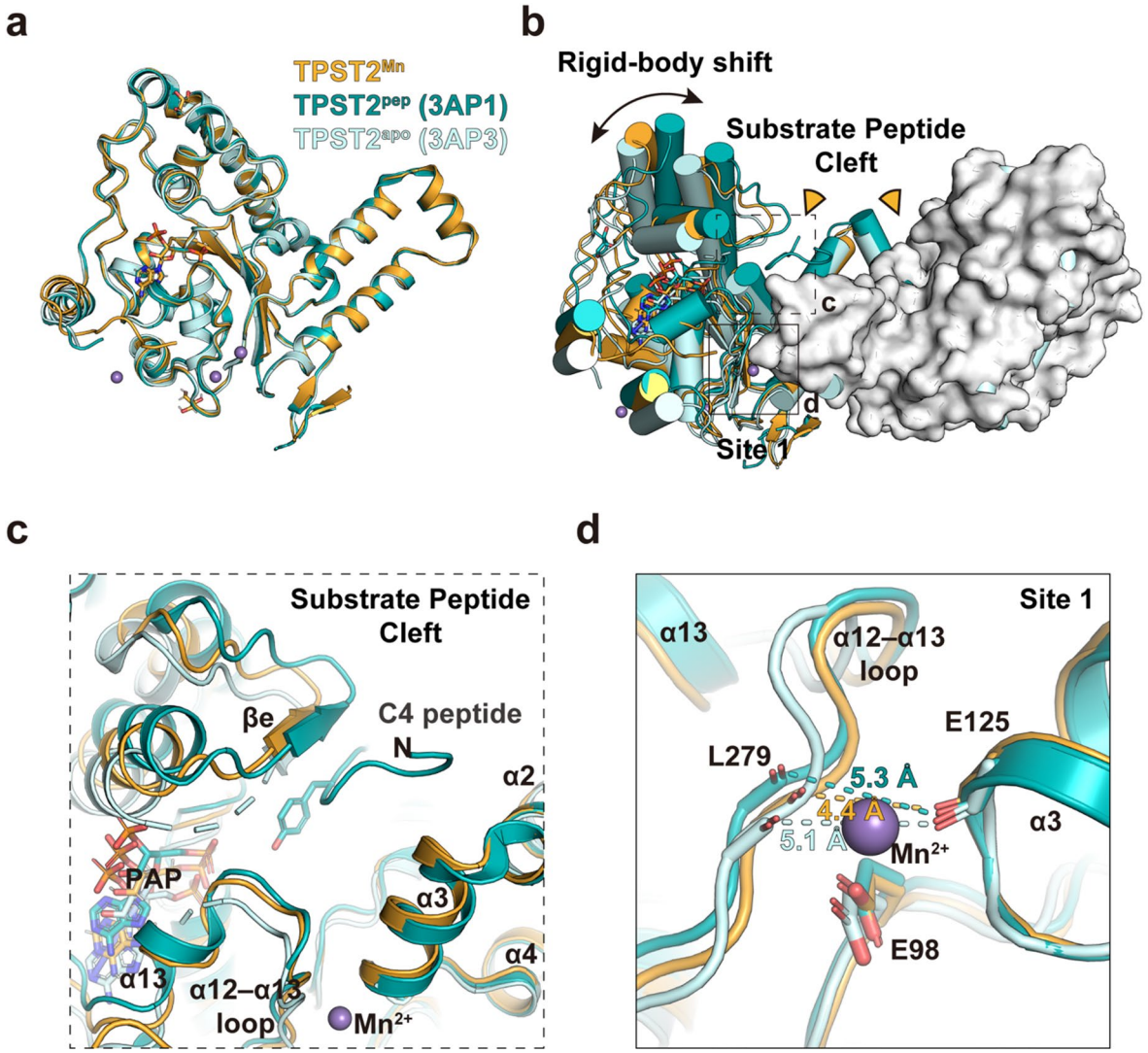

Fig. 5. Structural comparison of TPST2^{Mn} with TPST2^{apo} and TPST2^{pep}. (**a**) Cartoon representation of the superimposed TPST2^{Mn} (orange), TPST2^{pep} (teal; PDB 3AP1) and TPST2^{apo} (pale cyan; PDB 3AP3) monomers. Mn^{2+} ions are shown as light violet spheres. (**b**) Structural comparison of TPST2 dimers. Structures are aligned based on one protomer, which is shown as a surface representation. The rigid-body shift is indicated by a black arrow. The substrate peptide binding cleft is marked by an orange sector. (**c**) Close-up view of substrate peptide cleft in the superposed structures. PAP is shown as sticks in the nucleotide pocket, and the C4 peptide is shown as a cartoon with the acceptor tyrosine as stick. (**d**) Close-up view of cation-binding site 1 in the superposed structures. Mn^{2+} ions are shown as light violet spheres, and coordinating residues are represented as sticks. The distance between Glu125 and Leu279 is indicated by a dotted line and labeled.

	Human TPST2			Human TPST1		Tick TPST
RMSD (Å)	3AP1	3AP2	3AP3	5WRI	5WRJ	8W5Z
Monomer (A/B)	0.21/0.33	0.27/0.38	0.36/0.37	0.43/0.46	0.43/0.45	0.48/0.51
Dimer	0.65	0.91	0.61	1.81	1.55	0.66

Table 3. RMSD values between TPST^{Mn} and other TPSTs structures.

Gly275 at site 2 exhibited the most significant reductions upon Mn^{2+} binding. Both residues showed > 1.5σ fluctuations in the TPST2^{pep} structure relative to TPST2^{Mn}. Although not directly comparable due to its lower resolution, the TPST2^{apo} structure nevertheless displayed a high degree of flexibility in both regions with Z-RMSF values exceeding 2.0σ, which is similar to the TPST2^{pep} state (Supplementary Fig. 11a). Taken together, these results demonstrate that metal binding decreases the flexibility of the α3 helix and α12-α13 loop, consistent with the structural comparisons described above.

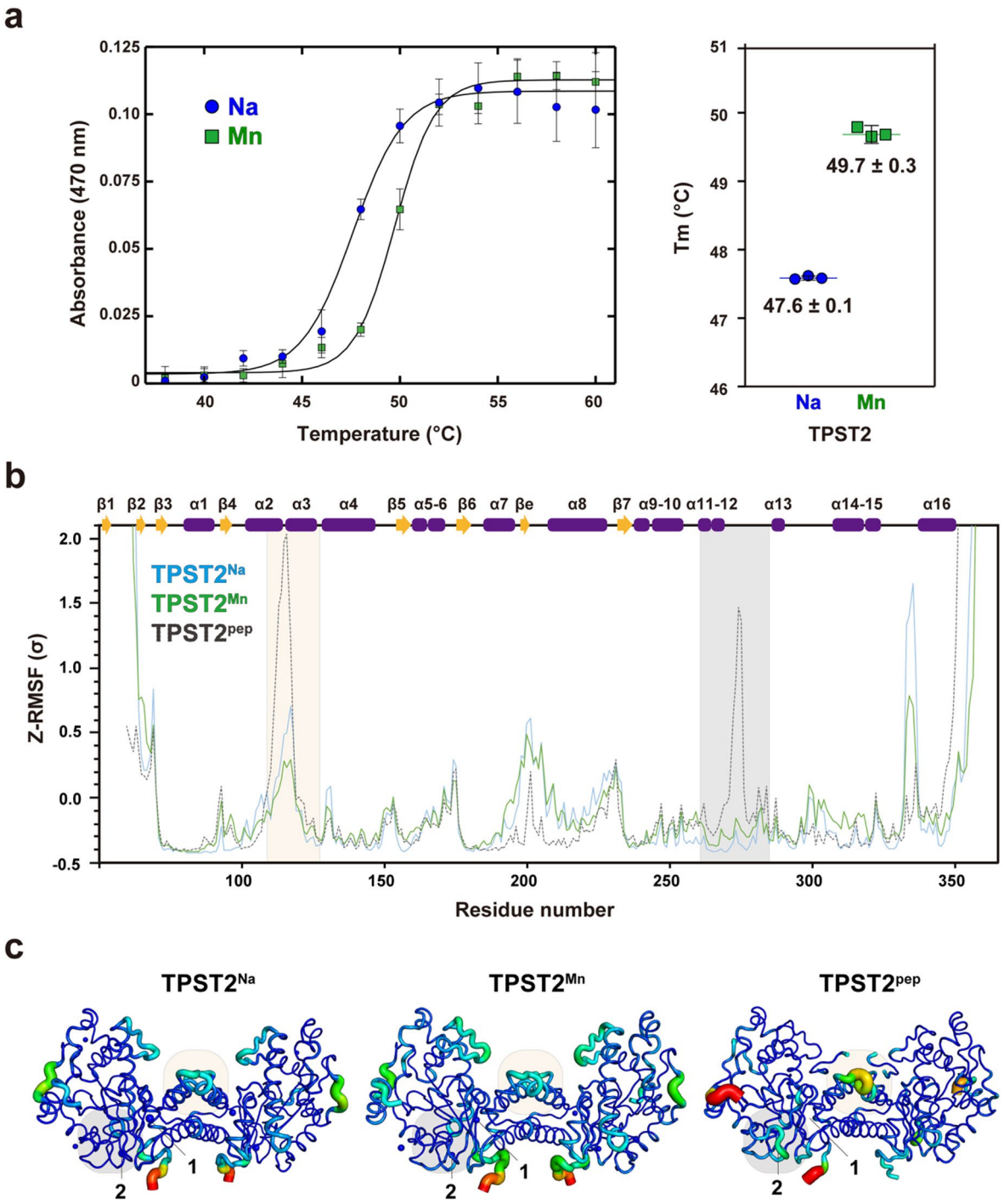

Fig. 6. Metal binding increases thermal stability and reduces local flexibility of TPST2. (**a**) Thermal-shift assay of TPST2 in Na^+ (blue) or Mn^{2+} (green). UV absorbance at 470 nm was measured across temperatures to determine T_m. Symbols show the mean ± 95% CI ($n = 3$). Dose-response curve fitting is shown as a black line. Calculated T_m values are indicated at right. **b** Per-residue Z-RMSF derived from ensemble refinement for $TPST2^{Na}$ (blue), $TPST2^{Mn}$ (green) and $TPST2^{pep}$ (grey). Secondary-structure elements are annotated above. Beige and gray shading marks regions where Z-RMSF values are lower in $TPST2^{Mn}$ than in $TPST2^{pep}$. **c** Representations of the RMSF based on ensemble refinements of $TPST2^{Na}$, $TPST2^{Mn}$ and $TPST2^{pep}$. Colors denote RMSF from 0 Å (blue) to 4 Å (red).

To complement the crystallographic analysis, we sampled TPST2 dynamics using BioEmu[33] and computed RMSF profiles across states (Supplementary Fig. 11b). Predicted flexible regions (RMSF > 2 Å) included the N-terminus (43–63), the α3-helix (112–131), the βe (196–202), the α12-α13 loop (272–296), and the C-terminus (339–359) (Supplementary Fig. 11c). These regions overlapped closely with ensemble-refined high Z-RMSF

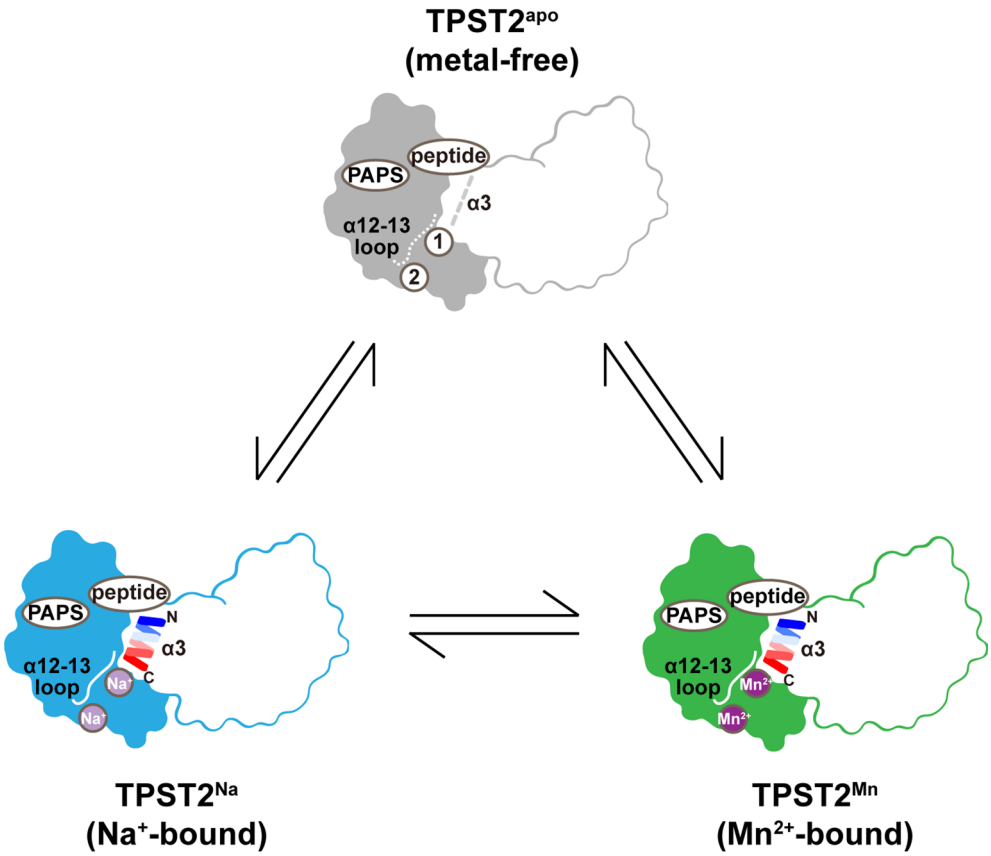

Fig. 7. Proposed model for metal-dependent activation of TPST2. The top panel shows a metal-free TPST2 state but no ordered cations at the two conserved sites. Binding of Na^+ (purple) to these sites stabilizes the α3 helix and the α12-α13 loop and yields a pre-organized conformation with modest catalytic activity. Binding of Mn^{2+} (light violet) further stabilizes these elements and corresponds to a more fully activated state that promotes efficient sulfation of acidic peptide substrates. Arrows indicate reversible association of Na^+ and Mn^{2+}.

regions from crystallography, especially the α3-helix and α12-α13 loop regions (Fig. 6b). Overall, our anomalous mapping, structural comparisons and ensemble-based dynamics analysis converge on a mechanism in which Mn^{2+} occupancy at the two octahedral sites reduces the flexibility of the α3-helix and the α12-α13 loop. This stabilization is reflected in the T_m and RMSF values and supports a model in which metal binding reduces conformational variability without inducing large conformational changes (Fig. 7).

Discussion

Protein tyrosine sulfation is a prevalent post-translational modification that regulates diverse extracellular signaling processes. TPSTs catalyze this reaction by transferring a sulfonyl group from PAPS to tyrosine residues, preferentially recognizing acidic motifs surrounding the target tyrosine (Fig. 1). Among the two human isoforms, TPST2 has been implicated in such physiological processes as thyroid hormone biosynthesis and reproduction as well as in pathological contexts that include tumor immune evasion and metastasis progression. Although TPST stimulation by divalent metals was first described decades ago, the molecular mechanism underlying this activation remained unresolved. In the present study, we identified two conserved metal-binding sites in TPST2 and demonstrated their structural and dynamic contributions to catalytic regulation.

Anomalous diffraction analysis revealed that Mn^{2+} is selectively bound to both metal-binding sites (Fig. 2b). Co^{2+} exhibited only weak binding, while Zn^{2+} and Cu^{2+} did not bind productively (Supplementary Figs. 8 and 9). The inability of Zn^{2+} to substitute for Mn^{2+} is consistent with its preference for tetrahedral coordination, which explains the lack of TPST2 activation by Zn^{2+} in biochemical assays. By contrast, Mn^{2+} stabilizes both the α3-helix at the dimer interface and the α12-α13 loop adjacent to the active site, which reduces conformational fluctuations and facilitates catalysis (Figs. 5 and 6). These findings provide a structural rationale for longstanding biochemical observations that Mn^{2+} strongly enhances TPST2 activity. Although Mg^{2+} has also been reported to activate TPST2 to a limited extent[25] and was present in our assay buffer, the structural analysis presented here focuses on Mn^{2+}-dependent activation. Because the Mn^{2+} concentrations in the Golgi lumen are thought to lie in the low-micromolar range, quantitative measurements of metal-binding affinities and site occupancy will be required to define how strongly TPST2 is activated under physiological conditions.

Direct comparison of the structures of Na^+- and Mn^{2+}-bound TPST2 showed that their overall conformations are nearly identical, indicating that metal-stimulated activity is not driven by large-scale rearrangements (Supplementary Fig. 10). Instead, stabilization occurs through modulation of local dynamics, particularly within the α3 segment and the α12-α13 loop. Using ensemble refinement, we observed that Mn^{2+} occupancy dampens fluctuations in these regions and that Na^+ binding produced a comparable stabilizing effect (Fig. 6b). Notably, previously reported TPST2 structures crystallized under high-NaCl conditions did not reveal clear ion densities[16]. This likely reflects partial occupancy or resolution limitations. By contrast, our Na^+-bound structure captured well-defined cation densities and a stabilized α3-helix, suggesting it represents a metal-stabilized form of TPST2 (Fig. 2d). These findings support an activation-by-ordering model in which a divalent metal, especially Mn^{2+}, reduces the entropic cost of catalysis by pre-organizing flexible structural elements at the active-site entrance (Fig. 7).

Together with thermal stability and dynamics analyses, these results support a model in which there are three metal-dependent states (Fig. 7). In the metal-free state, the α3-helix and α12-α13 loop remain flexible and the enzyme lacks full catalytic competence. Under Na^+-rich conditions, Na^+ can occupy the two octahedral sites at sufficient occupancy to promote partial ordering of the α3-helix. This metal-stabilized form of TPST2 likely represents a partially activated conformation in which structural elements are restrained but catalytic efficiency remains modest due to the weak coordination strength of monovalent ions. Full activation occurs upon the binding of Mn^{2+} (or Co^{2+}), which engage both sites with stronger coordination geometry. This stabilizes the α3-helix dipole and the α12-α13 loop more effectively, lowering the entropic barrier for catalysis and priming the enzyme for recognition of acidic peptide substrates. Thus, metal binding does not induce large conformational transitions but shifts TPST2 toward an ordered, catalytically competent state by stabilizing local elements at the active-site entrance. The precise order of PAP/PAPS and metal binding during this cycle remains unresolved; future kinetic and thermodynamic studies will be needed to clarify how metal ions modulate cofactor and substrate recognition by TPST2 and to delineate the potential contribution of each of the cation-binding sites.

Beyond their structural significance, these findings carry potential physiological and pathological implications. TPST2 activity has been shown to modulate interferon receptor signaling in melanoma and to stabilize integrin β4 in pancreatic cancer, thereby promoting immune evasion and metastatic progression[26,27]. Our results suggest that local metal ion availability, particularly the Mn^{2+} concentration within the Golgi lumen, may directly influence TPST2 activity in cells. Other studies indicate that the Golgi apparatus functions as a major intracellular Mn^{2+} store and that the luminal Mn^{2+} pool is enriched but tightly controlled in the low-micromolar range, where small changes are sufficient to modulate Mn^{2+}-dependent enzymes and glycosylation[34–37]. Perturbations in Mn^{2+} homeostasis, which have been associated with metabolic disorders and cancer, could therefore intersect with TPST2-mediated pathways and contribute to disease outcomes. This possibility highlights a regulatory axis linking cellular ion balance with extracellular signaling via protein sulfation. In addition, our comparative analysis suggests that conservation of the metal-binding sites varies among species, implying that the extent of metal-dependent regulation may not be universal and warrants further investigation.

In summary, we determined the structural basis of metal binding in human TPST2 and revealed that Mn^{2+} occupancy enhances enzyme activity by stabilizing flexible elements near the active site. This dynamics-centered mechanism explains the metal dependence of TPST2 and rationalizes the selective activation by Mn^{2+}. These findings integrate structural, biochemical, and pathological perspectives, establishing a foundation for future studies on how TPST2 couples metal ion regulation to extracellular signaling and disease processes.

Materials and methods

Cloning, expression, and purification of *h*TPST2

Human TPST2 (*h*TPST2, residues 43–459, UniProt ID: O60704) was codon-optimized for *Escherichia coli* and synthesized (GenScript). *h*TPST2 was subcloned into modified pET23b (Novagen) vector containing an N-terminal His6-tag and maltose binding protein (MBP) followed by a TEV protease cleavage site. The recombinant vectors were transformed into Rosetta-gami 2 (DE3) pLysS cells, which were then grown in Luria-Bertani (LB) medium containing 50 μg/mL kanamycin at 37 °C until the UV absorbance at 600 nm was 0.6. Recombinant proteins were expressed under induction with 0.5 mM isopropyl-D-thiogalactoside (IPTG) at 20 °C for 20 h.

Cells were harvested and lysed by sonication in buffer A [50 mM Tris-HCl (pH 7.5), 500 mM NaCl, 40 mM imidazole, 5 mM β-mercaptoethanol (β-ME), 0.3% (*v*/*v*) Triton X-100 and 1 mM phenylmethylsulfonyl fluoride]. Clarified lysates were centrifuged at 15,184 x g at 4 °C for 1 h., after which the supernatant was collected and applied to an Econo-Cloumn (Bio-Rad) packed with Ni-NTA agarose resin pre-equilibrated with buffer A. After washing with buffer A, protein was eluted with buffer B [50 mM Tris-HCl (pH 7.5), 500 mM NaCl, 500 mM imidazole and 5 mM β-ME]. The eluted protein was concentrated to 2 mg/mL using an Amicon Ultra-15 50 K (Millipore, Merck), and the His6-MBP tag was cleaved with TEV protease at 4 °C for 14 h along with dialysis against buffer C [20 mM Tris-HCl (pH 8.0), 300 mM NaCl and 5 mM β-ME]. After dialysis, *h*TPST2 were eluted using increasing concentrations of imidazole in buffer C in a second NI-NTA affinity chromatography step. The fractions containing the *h*TPST2 were collected and concentrated using an Amicon Ultra-15 30 K (Millipore, Merck) followed by sodium dodecyl sulfate polyacrylamide gel electrophoresis (SDS-PAGE). *h*TPST2 was then subjected to size-exclusion chromatography (SEC) on a HiLoad 16/60 Superdex 75 prep grade column (Pharmacia) pre-equilibrated with buffer D [20 mM Tris-HCl (pH 7.5), 100 mM NaCl]. The peak fractions were collected, concentrated to 2.2 mg/mL and stored at − 80 °C.

Crystallization and soaking experiments

Prior to crystallization, PAP was added to the purified *h*TPST2 to a final concentration of 0.5 mM and incubated on ice for 30 min. Initial crystallization screening was carried out using the sitting-drop vapor diffusion method

at 20 °C in a 96-well INTELLI-PLATE (Art Robbins Ins.). Drops were prepared by mixing 0.2 µL of *h*TPST2 (2.0 mg/mL) and 0.2 µL of reservoir solution. Microcrystals formed after 3 days in Pact premier 1 & 2 Screen C12 [0.1 M HEPES-NaOH (pH 7.0), 20% (*w*/*v*) PEG 6000 and 10 mM $ZnCl_2$] reservoir solution. Additional crystallization trials were performed using a 24-well Cryscheme plate (Hampton) by mixing 2 µL of protein and 2 µL of reservoir solution. Optimized $TPST2^{Na}$ and $TPST2^{Mn}$ crystals were respectively obtained in reservoir solutions containing 0.1 M HEPES-NaOH (pH 7.0), 16% (*w*/*v*) PEG 6000, 25 mM $ZnCl_2$ and 0.1 M potassium sodium tartrate or in 0.1 M HEPES-NaOH (pH 7.0), 14.2% (*w*/*v*) PEG 6000, 1 mM $ZnCl_2$, 20 mM $MnCl_2$ and 0.1 M potassium sodium tartrate. Crystals were cryoprotected in mother liquor supplemented with 20% (*w*/*v*) glycerol before flash freezing in liquid nitrogen.

Data collection, structure determination, and refinement.

Diffraction data were collected at 100 K using a synchrotron X-ray source on beamlines 5 C and 11 C at the Pohang Accelerator Laboratory (PAL) (Pohang, Korea). The best resolution diffraction data for $TPST2^{Na}$ and $TPST2^{Mn}$ were collected at 1.75 Å and 2.00 Å resolution, respectively. Diffraction data were collected at wavelengths of 1.0000 Å ($TPST^{Na}$), 0.9794 Å ($TPST^{Mn}$), 1.8933 Å (Mn K-edge), and additional energies corresponding to the Co, Zn and Cu K-edges. Data indexing, integration and scaling were performed using XDS package[38] and HKL suite[39]. All crystals were in the tetragonal space group $P4_122$. Structures were solved using molecular replacement with Phaser-MR[40] in the PHENIX package[41] with TPST2 (PDB ID: 3AP1) as the template. Iterative refinement was performed with *phenix.refine* in the PHENIX package and REFMAC5 in the CCP4i suite[42], and model building was carried out in Coot[43]. The coordinates and structural factors were deposited in the PDB RCSB with an accession code of 9WWE for $TPST2^{Na}$ and 9WWF for $TPST2^{Mn}$.

Soaking and anomalous x-ray diffraction data collection.

Pre-grown $TPST2^{Na}$ crystals were transferred into soaking solution [0.1 M HEPES-NaOH pH 7.0, 16% (*w*/*v*) PEG 6000, 1 mM $ZnCl_2$ and 0.1 M potassium sodium tartrate] supplemented with 10 mM $CoCl_2$, $ZnCl_2$, or $CuCl_2$ for 30 min to 3 h at 20 °C. After soaking, crystals were briefly back-soaked in reservoir solution before cryo-cooling.

To confirm metal binding, single-wavelength anomalous diffraction (SAD) data were collected at the respective K-edge peak wavelengths of Mn (λ = 1.8933 Å), Co (λ = 1.6054 Å), Zn (λ = 1.2824 Å), and Cu (λ = 1.3785 Å). Diffraction data sets [data titles: Mn (ano), Co (ano), Zn (ano), Cu (ano)] were indexed, integrated and scaled using the HKL suite and XDS package. Molecular replacement was carried out with Phaser-MR in the PHENIX package using the $TPST2^{Na}$ structure (PDB ID: 9WWE) as the search model. Anomalous difference Fourier maps were calculated with *phenix.maps* and subsequently inspected in Coot to identify the bound metal ions. Details of the data collection statistics are summarized in Table 1.

Structural analysis

PyMOL[44] version 2.5.0 was used for all structural analyses and figures. Multiple sequence alignment was performed using Jalview[45], with multiple alignment and conservation analyses executed through the JABAWS web service framework[46,47]. Metal-binding geometries were assessed and the cation assignments validated using the CheckMyMetal[31] (CMM) and MetalPDB[32] servers; full CMM reports for each site and condition are provided in Supplementary Fig. 6. Interface areas and oligomerization states were analyzed with PDBePISA[48].

Ensemble refinement and RMSF analysis

Ensemble refinement of TPST2 structures was carried out with *phenix.ensemble_refinement*[49], using structure factors and coordinates as input. The simulations comprised an equilibration phase of 6 ps (10 τ_x periods, 1200 macro cycles), during which temperature, X-ray weight and averaged structure factors stabilized, followed by an acquisition phase of 12 ps (20 τ_x periods, 2400 macro cycles). The combined 18 ps trajectories were used to generate ensemble models. RMSF values were calculated from the ensemble coordinates. To normalize structural fluctuations and allow chain-wise comparison, we additionally computed Z-RMSF values, defined as residue-wise RMSF values standardized by subtracting the mean and dividing by the standard deviation across all residues[50]. The ensembles were visualized in PyMOL (v2.5.0) using *ens_tool.py*.

BioEmu analysis

BioEmu[33] was employed to generate equilibrium ensembles of TPST2 using the ColabFold[51] BioEmu notebook. A total of 1000 structural samples were generated using its diffusion-based sampling protocol. Residue-wise RMSF values were computed from the BioEmu ensembles.

Thermal stability assay

The melting temperature of *h*TPST2 was determined spectrophotometrically as described previously[52]. Briefly, 50 µL of 50 µM purified protein in buffer D were introduced into PER tubes, and the temperature was raised at a rate of 4 °C per 90 s using a Thermal Cycler Dice Gradient (Takara Bio, Inc). Turbidity was quantified by measuring absorbance at 470 nm with a Nanodrop-2000 spectrophotometer (Thermo Fisher Scientific, Inc). The dose-response curve was fitted using Veusz 4.1. All experiments were conducted in triplicate (n = 3). Data are presented as the mean ± 95% confidence interval (CI).

Evaluation of *h*TPST2 enzyme activity.

Enzyme activity of *h*TPST2 was assayed as described previously[53]. *h*TPST2 activity was measured using a Universal Sulfotransferase Activity Kit (R&D Systems, EA003). The reaction buffer contained 50 mM Tris-HCl (pH 7.0), 15 mM $MgCl_2$, 20 mM NaCl, 0.75 mg/mL BSA, and 0.1% Triton X-100. Reaction mixtures containing TPST2 (30

nM), PAPS (100 μM; R&D Systems, ES019), C4 peptide substrate (100 μM; Chempeptide, EDFEDYEFD), and IMPAD1 (10 ng/μL; R&D Systems, EA003) were prepared and dispensed into a 96-well clear-bottom plate (SPL, 31096) at 50 μL per well. The plate was then incubated at 20 °C for 0–5 h. After incubation, 160 μL of a freshly prepared mixture of Malachite Green Reagent A, distilled water, and Reagent B [3:10:3 (v/v); R&D Systems, EA003] was added to each well and incubated for an additional 1 h at 20 °C. Absorbance was measured at 630 nm using a FlexStation 3 Multimode Microplate Reader (Molecular Devices). The amount of phosphate produced was determined from the absorbance values using a standard curve generated with phosphate standard solutions (R&D Systems, EA003).

Statistics and reproducibility

All biochemical assays were performed in at least three independent replicates. Thermal shift assay data are presented as the mean ± 95% confidence interval (CI), and enzymatic activity data as the mean ± standard error of the mean (SEM). Structural refinements and RMSF analyses were reproduced with independent datasets.

Data availability

The coordinates and structural factors for TPST2 Na and TPST2 Mn have been deposited in the Protein Data Bank under accession codes 9WWE and 9WWF (PDB DOI: https://doi.org/10.2210/pdb9WWE/pdb and https://doi.org/10.2210/pdb9WWF/pdb). The source data underlying the graphs presented in the paper are provided in Supplementary Data 1. All other data are available from the corresponding author upon reasonable request.

Received: 22 October 2025; Accepted: 20 January 2026
Published online: 23 January 2026

6. References

1. Lee, R. & Huttner, W. Tyrosine-O-sulfated proteins of PC12 pheochromocytoma cells and their sulfation by a tyrosylprotein sulfotransferase. *J. Biol. Chem.* **258**, 11326–11334 (1983).
2. Baeuerle, P. A. & Huttner, W. B. Tyrosine sulfation is a trans-Golgi-specific protein modification. *J. Cell. Biol.* **105**, 2655–2664 (1987).
3. Huttner, W. B. Tyrosine sulfation and the secretory pathway. *Annu. Rev. Physiol.* **50**, 363–376 (1988).
4. Lipmann, F. Biological sulfate activation and transfer: studies on a mechanism of group activation and its role in biosynthesis are described. *Science* **128**, 575–580 (1958).
5. Yang, Y. S. et al. Tyrosine sulfation as a protein post-translational modification. *Molecules* **20**, 2138–2164 (2015).
6. Hille, A., Braulke, T., von FIGURA, K. & Huttner, W. B. Occurrence of tyrosine sulfate in proteins–a balance sheet: 1. Secretory and lysosomal proteins. *Eur. J. Biochem.* **188**, 577–586 (1990).
7. Hille, A. & Huttner, W. B. Occurrence of tyrosine sulfate in proteins–a balance sheet: 2. Membrane proteins. *Eur. J. Biochem.* **188**, 587–596 (1990).
8. Kehoe, J. W. & Bertozzi, C. R. Tyrosine sulfation: a modulator of extracellular protein–protein interactions. *Chem. Biol.* **7**, R57–R61 (2000).
9. Huttner, W. B. Sulphation of tyrosine residues—a widespread modification of proteins. *Nature* **299**, 273–276 (1982).
10. Moore, K. L. The biology and enzymology of protein tyrosine O-sulfation. *J. Biol. Chem.* **278**, 24243–24246 (2003).
11. Stewart, V. & Ronald, P. C. Sulfotyrosine residues: interaction specificity determinants for extracellular protein–protein interactions. *J. Biol. Chem.* **298**, 102232 (2022).
12. Ouyang, Y., Lane, W. S. & Moore, K. L. Tyrosylprotein sulfotransferase: purification and molecular cloning of an enzyme that catalyzes tyrosine O-sulfation, a common posttranslational modification of eukaryotic proteins. *Proc. Natl. Acad. Sci. USA*. **95**, 2896–2901 (1998).
13. Beisswanger, R. et al. Existence of distinct tyrosylprotein sulfotransferase genes: molecular characterization of tyrosylprotein sulfotransferase-2. *Proc. Natl. Acad. Sci. USA*. **95**, 11134–11139 (1998).
14. Ouyang, Y. B. & Moore, K. L. Molecular cloning and expression of human and mouse tyrosylprotein sulfotransferase-2 and a tyrosylprotein sulfotransferase homologue in caenorhabditis elegans. *J. Biol. Chem.* **273**, 24770–24774 (1998).
15. Kakuta, Y., Pedersen, L. G., Pedersen, L. C. & Negishi, M. Conserved structural motifs in the sulfotransferase family. *Trends Biochem. Sci.* **23**, 129–130 (1998).
16. Teramoto, T. et al. Crystal structure of human tyrosylprotein sulfotransferase-2 reveals the mechanism of protein tyrosine sulfation reaction. *Nat. Commun.* **4**, 1572 (2013).
17. Tanaka, S. et al. Structural basis for the broad substrate specificity of the human tyrosylprotein sulfotransferase-1. *Sci. Rep.* **7**, 8776 (2017).
18. Lee, R. & Huttner, W. B. $(Glu^{62}, Ala^{30}, Tyr^{8})_n$ serves as high-affinity substrate for tyrosylprotein sulfotransferase: a Golgi enzyme. *Proc. Natl. Acad. Sci. USA* **82**, 6143–6147 (1985).
19. Niehrs, C. & Huttner, W. B. Purification and characterization of tyrosylprotein sulfotransferase. *EMBO J.* **9**, 35–42 (1990).
20. Bundgaard, J. R., Vuust, J. & Rehfeld, J. F. New consensus features for tyrosine O-sulfation determined by mutational analysis. *J. Biol. Chem.* **272**, 21700–21705 (1997).
21. Yoshimura, M. et al. Crystal structure of tick tyrosylprotein sulfotransferase reveals the activation mechanism of the tick anticoagulant protein Madanin. *J Biol. Chem.* **300** (2024).
22. Westmuckett, A. D., Hoffhines, A. J., Borghei, A. & Moore, K. L. Early postnatal pulmonary failure and primary hypothyroidism in mice with combined TPST-1 and TPST-2 deficiency. *Gen. Comp. Endocrinol.* **156**, 145–153 (2008).
23. Borghei, A. et al. Targeted disruption of tyrosylprotein sulfotransferase-2, an enzyme that catalyzes post-translational protein tyrosine O-sulfation, causes male infertility. *J. Biol. Chem.* **281**, 9423–9431 (2006).
24. Sasaki, N. et al. A mutation in Tpst2 encoding tyrosylprotein sulfotransferase causes dwarfism associated with hypothyroidism. *Mol. Endocrinol.* **21**, 1713–1721 (2007).
25. Mishiro, E., Sakakibara, Y., Liu, M. C. & Suiko, M. Differential enzymatic characteristics and tissue-specific expression of human TPST-1 and TPST-2. *J. Biochem.* **140**, 731–737 (2006).
26. Oh, Y. et al. Genome-wide CRISPR screening identifies tyrosylprotein sulfotransferase-2 as a target for augmenting anti-PD1 efficacy. *Mol. Cancer.* **23**, 155 (2024).
27. Cai, X. et al. Inhibition of the SLC35B2-TPST2 axis of tyrosine sulfation attenuates the growth and metastasis of pancreatic ductal adenocarcinom. *Cell. Mol. Gastroenterol. Hepatol.* **16**, 473–495 (2023).
28. Ujiie, K. et al. Specific recognition mechanism of an antibody to sulfated tyrosine and its potential use in biological research. *J. Biol. Chem.* **301** (2025).

29. Kasinathan, C., Rizwan, M., Slomiany, A. & Slomiany, B. L. Effect of sofalcone on tyrosylprotein sulfotransferase. *Gen. Pharmacol.* **25**, 1017–1020 (1994).
30. Byrne, D. P. et al. New tools for evaluating protein tyrosine sulfation: tyrosylprotein sulfotransferases (TPSTs) are novel targets for RAF protein kinase inhibitors. *Biochem. J.* **475**, 2435–2455 (2018).
31. Gucwa, M. et al. CMM—An enhanced platform for interactive validation of metal binding sites. *Protein Sci.* **32**, e4525 (2023).
32. Putignano, V., Rosato, A., Banci, L. & Andreini, C. MetalPDB in 2018: a database of metal sites in biological macromolecular structures. *Nucleic Acids Res.* **46**, D459–D464 (2018).
33. Lewis, S. et al. Scalable emulation of protein equilibrium ensembles with generative deep learning. *Science* **389**, eadv9817 (2025).
34. Das, S. et al. Manganese mapping using a fluorescent Mn^{2+} sensor and Nanosynchrotron X-ray fluorescence reveals the role of the golgi apparatus as a manganese storage site. *Inorg. Chem.* **58** (20), 13724–13732 (2019).
35. Potelle, S. et al. Glycosylation abnormalities in Gdt1p/TMEM165 deficient cells result from a defect in golgi manganese homeostasis. *Hum. Mol. Genet.* **25** (8), 1489–1500 (2016).
36. Potelle, S. et al. Manganese-induced turnover of TMEM165. *Biochem. J.* **474** (9), 1481–1493 (2017).
37. Jankauskas, S. S. et al. Insights into molecular and cellular functions of the golgi calcium/manganese-proton antiporter TMEM165. *J. Biol. Chem.* **300** (8), 107567 (2024).
38. Kabsch, W. *Acta Crystallogr. Sect. D Biol. Crystallogr.* **66**, 125–132 (2010).
39. Otwinowski, Z. & Minor, W. *Methods Enzymol.* **276**, 307–326 (1997).
40. McCoy, A. J. et al. Phaser crystallographic software. *J. Appl. Crystallogr.* **40**, 658–674 (2007).
41. Liebschner, D. et al. Macromolecular structure determination using X-rays, neutrons and electrons: recent developments in phenix. *Acta Crystallogr. Sect. D Struct. Biol.* **75**, 861–877 (2019).
42. Agirre, J. et al. The CCP4 suite: integrative software for macromolecular crystallography. *Acta Crystallogr. Sect. D Struct. Biol.* **79**, 449–461 (2023).
43. Emsley, P., Lohkamp, B., Scott, W. G. & Cowtan, K. Features and development of Coot. *Acta Crystallogr. Sect. D Biol. Crystallogr.* **66**, 486–501 (2010).
44. Schrodinger, L. The PyMOL molecular graphics system. *Version* **1**, 8 (2015).
45. Waterhouse, A. M., Procter, J. B., Martin, D. M., Clamp, M. & Barton, G. J. Jalview version 2—a multiple sequence alignment editor and analysis workbench. *Bioinformatics* **25**, 1189–1191 (2009).
46. Troshin, P. V., Procter, J. B. & Barton, G. J. Java bioinformatics analysis web services for multiple sequence alignment—JABAWS. *MSA Bioinformatics*. **27**, 2001–2002 (2011).
47. Troshin, P. V. et al. JABAWS 2.2 distributed web services for bioinformatics: protein disorder, conservation and RNA secondary structure. *Bioinformatics* **34**, 1939–1940 (2018).
48. Krissinel, E. & Henrick, K. Inference of macromolecular assemblies from crystalline state. *J. Mol. Biol.* **372**, 774–797 (2007).
49. Burnley, B. T., Afonine, P. V., Adams, P. D. & Gros, P. Modelling dynamics in protein crystal structures by ensemble refinement. *Elife* **1**, e00311 (2012).
50. Song, X. et al. Accurate prediction of protein structural flexibility by deep learning integrating intricate atomic structures and Cryo-EM density information. *Nat. Commun.* **15**, 5538 (2024).
51. Mirdita, M. et al. ColabFold: making protein folding accessible to all. *Nat. Methods*. **19**, 679–682 (2022).
52. Jin, M., Yang, J., Park, J., Kim, H. & Eom, S. H. Structure of MICU from non-metazoan dictyostelium discoideum reveals unique characteristics. *Commun. Biol.* **8**, 782 (2025).
53. Park, S. B. et al. Discovery of (4-Phenyl-cyclohexyl) acetate-Derived tyrosylprotein sulfotransferase 2 (TPST2) inhibitors with potent anti-tumor activity for immuno-oncology applications. *J. Med. Chem.* (2025).

Acknowledgements

We gratefully acknowledge the staff at beamlines BL-5 C and 11 C at the PAL for their kind help with data collection. This research was supported by the National Research Foundation (NRF) of the Korean government (NRF-2021R1A2C1006267) and by the Bio&Medical Technology Development Program of the National Research Foundation (NRF) funded by the Korean government (RS-2024-00344154 and RS-2024-00440614).

Author contributions

S.H.E. and M.J. conceived the study and organized experiments; M.J. performed most experiments; C.N., J.Y., and H.K. contributed to X-ray diffraction experiments and data analysis; S.B.P. contributed to enzyme activity assays and analysis; S.H.E. and Y.C.K. provided advice and guidance. All authors contributed to the interpretation of the results and preparation of the manuscript.

Funding

This research was supported by the National Research Foundation (NRF) of the Korean government (NRF-2021R1A2C1006267) and by the Bio&Medical Technology Development Program of the National Research Foundation (NRF) funded by the Korean government (RS-2024-00344154 and RS-2024-00440614).

Declarations

Competing interests

The authors declare no competing interests.

Additional information

Supplementary Information The online version contains supplementary material available at https://doi.org/10.1038/s41598-026-37189-4.

Correspondence and requests for materials should be addressed to S.H.E.